

Utilisation of ash fractions from phosphorus-rich residual streams

Main applicant: Anna Strandberg, Swedish University of Agricultural Sciences

Co-applicants: Mikael Thyrel, Swedish University of Agricultural Sciences

Sylvia Larsson, Swedish University of Agricultural Sciences

Nils Skoglund, Umeå University

Summary of Results

Two types of sludges from a paper mill has been co-combusted with bark, with two different degrees of admixture for respective sludge. The amount of P in the slag particles indicate that the ash from biosludge and mixed sludge combustion can be useful either as a soil improver directly or for a further refinery. Slag from the combustion of 30_{wt%} biosludge and 70_{wt%} bark contained the highest content of phosphorus, 9_{at%} on a C and O free basis, followed by 10_{wt%} biosludge and 90_{wt%} bark (6.2_{at%}) and 30_{wt%} mixed sludge and 70_{wt%} bark (5.8_{at%}).

Morphology of slag particles was analysed with synchrotron-based X-ray micro-tomography and image analysis. Discrete and open pores could be distinguished on a micrometre scale. The bark och sludge mixtures had comparable porosity (18-23_{vol%}) and had an open pore volume of 39 to 48_{vol%}. Slag from the combustion of pure bark had lower porosity (12_{vol%}) and lowered open pore volume (12_{vol%}). For all samples, 90% of the pores are small, with an equivalent diameter under 30 µm, but the largest pore volume (80-90%) consists of pores with an equivalent diameter over 75 µm. In soils, pores with a minimum equivalent diameter over 30 µm generally transmit water and the smaller pores store water.

Overall, the slag particles have many small discrete pores and relatively thick walls, with few pore openings to the surroundings, indicating that slag particles need to be grounded before application in the soil for improving root access to the nutrients.

Introduction

Phosphorus (P) is vital for all living organisms. Today, the recycling of P is low, and the supply comes mainly from phosphate rocks and minerals. The European Commission has also identified P as critical raw material [1]. For a sustainable society, it is crucial to recover P from bio-resources and residual streams.

With pulp and paper production in the world of 420 million tonnes (2018), the pulp and paper industry is a large industry sector (CEPI 2019 [2]). The production also results in several residual

streams, amongst which sludges in different forms are produced to a large amount in the wastewater treatment plants. Landfilling has been, and still is in many places, a common way to treat the sludge after dewatering, but more stringent regulations promote material and energy recovery [3, 4].

Through the combustion of phosphorus-rich residual streams, it is possible to utilise, among other things, the phosphorus-bound fraction in the produced ash for further reprocessing and recycling of nutrients, and at the same time recover the energy [5-9]. It has also been found to partially control combustion processes whereby elements that are not suitable for recycling (e.g. copper and lead) end up in a finer-grained and particulate ash fraction, where most phosphorus compounds are not found [10].

The purpose of the study was to contribute to a circular society by investigating possibilities for utilising nutrient-rich ash fractions from the combustion of five different fuel compositions consisting of bark and two types of sludges, which are residuals streams from the bioenergy sector and from pulp and paper mills. The combustion performance was investigated for these residual streams, and advanced analysis methods were used to characterise the ashes and link together chemical and physical properties relevant for nutrient recycling of the ashes. The elemental composition of ash fractions was evaluated by energy dispersive X-ray fluorescence (ED-XRF) and energy-dispersive X-ray spectroscopy (SEM-EDS), and crystalline phases by X-ray diffraction (XRD) of the samples. Morphology, porosity, pore size distribution and active surface area of the slag were characterised with synchrotron-based X-ray micro-tomography (XRT).

Experimental Methods

Materials and pre-treatment

Two types of sludges from a paper mill in Hallstavik, Sweden, was used in this study, mixed sludge and biological sludge. Mixed sludge contains fibre sludge (fibre residues and some inert material) and about 30-35 % biological sludge. The sludges also contain Ferrous sulphate (approx. 15 kg/ton). The biosludge has higher ash content (16.9 wt%) than mixed sludge (7.0 wt%) on a dry basis. The mixed sludge contains relatively much more Si compared to the biosludge. The sludges were dried at 105°C and grounded with a 5-mm sieve.

The bark used in this study was Scots pine bark that came from a sawmill in Northern Sweden. The bark was ground with a 4-mm sieve.

Five fuel mixtures were used and designed based on the composition of the ash forming elements in the fuel and practical issues due to the high ash content in the sludges. The fuels were 100 % bark (B100), 10 wt% mixed sludge and 90 wt% bark (MSB90), 30 wt% mixed sludge and 70 wt% bark (MSB70), 10 wt% biosludge and 90 wt% bark (BSB90), and 30 wt% biosludge and 70 wt% bark (BSB70). The fuels were pelletised in a pilot-scale pellet press with a stationary Ø8 mm ring die. The fuels and the pellets were analysed in an accredited laboratory for ash content, main elements C, H, N, Cl and S and ash-forming elements (26 trace metals in biofuels).

Combustion experiments

Combustion experiments have been performed in a horizontal underfed pellet burner (Ecotec BioLine 50), installed in a boiler (Eryl, Falun, Sweden), with an integrated water-cooled heat exchanger. A detailed description is available elsewhere [11]. The combustion experiments lasted 4-6 hours, starting with stem wood pellets until a steady state was reached. After that, respective pellet sorts were fed with an 8.5 kg/h for bark and 8.8-9.4 kg/h for the mixed fuels. During combustion, the temperature in and just above the burner grate and the O₂, CO₂, CO, NO, NO₂ and SO₂ in the flue gas was measured continuously.

The ash residues were collected after the boiler had cooled down and were sieved and quantified. The ashes were separated between ash in burner grate and bottom ash, and after size fraction: slag particles from the burner grate at a size larger than 3.15 mm, particles in the burner grate at a size of 1.4-3.15 mm, non-melted ash in the burner under the size of 1.4 mm, non-melted ash particles larger than 3.15 mm at the bottom of the boiler (bottom ash), bottom ash particles at a size of 1.4-3.15 mm, and bottom ash under the size of 1.4 mm. No fly ash was found in the fly ash hopper, but deposits were collected from the heat exchanger.

Ash characterisation

Elemental composition

Elemental investigation of the ash fractions was performed with Energy-dispersive X-ray fluorescence (ED-XRF). A Niton XL3t energy-dispersive XRF analyser (Thermo Scientific Niton, Billerica, MA, USA) collected spectra. Before analyses, samples over 1.4 mm were grounded.

A variable-pressure scanning electron microscope with an energy-dispersive X-ray spectroscope (SEM-EDS; Carl Zeiss Evo and Oxford instruments, detector X-Max 80 mm²) was also used to determine the elemental composition at low vacuum mode at 50 Pa. A beam accelerating voltage of 15 kV and probe current of 750 pA was used. A part of the powdery samples was transferred to carbon tape, and three replicates from each ash fraction were analysed. Four area analyses were performed (1.5 mm × 1.1 mm) on each sample, giving 12 analyses in total for each ash fraction.

Powder X-ray diffraction (XRD)

XRD analysis was performed with a Bruker-AXS D8Advance X-ray diffractometer in θ - θ mode for identification and semi-quantitative distribution of crystalline compounds. Cu-K α radiation and a Vântec-1 detector were used with continuous rotating scans in a range from 10° to 70°. Collected diffractograms were evaluated with the PDF-4+ database in Diffrac.EVA 4.2.

X-ray microtomography and image analysis

The X-ray microtomography imaging was performed on slag particles at the beamline Anatomix, of Synchrotron SOLEIL, France [12]], with an electron beam current of 100 mA in the storage ring. The polychromatic ('white') X-ray beam used for the measurements had a central photon energy of around 40 keV. The samples, mounted on a rotating stage, were scanned over a range of 180 degrees respective 360 degrees for samples not fitting inside the field of view, with a field of view of 6.5 mm and a pixel size of 3.07 μ m. 1600-5900 projections were collected on each scan with an ORCA Flash 4.0 V2 digital camera, 2 x magnification lens, and 10-50 ms exposure time. Three slag particles from each combustion experiment were scanned, and 2-3 scans were added vertically to cover each particle.

The software PyHST2 [13] with a filtered back-projection algorithm was used for reconstruction. A double flatfield algorithm was used to reduce ring artefacts, and a Paganin filter was used for semi-quantitative phase retrieval [14, 15].

The data analysis was performed on the reconstructed 3D stack of image files at 8-bit with the software packages Fiji (Fiji Is Just ImageJ) [16, 17] and Avizo 9.3 (Fei VSG Inc., Burlington, MA, USA). Each voxel contains a grayscale value corresponding to the X-ray attenuation (0-255 for 8-bit images). The X-ray attenuation depends on the differences in density and the atomic number of the elements in the object. Dark levels in the images are areas with low attenuation (low number on grayscale), such as pores and air, and bright levels are the ash with the highest attenuation for iron-rich melts (see Figure 1).

Porosity, open-pore volume, pore size distribution, the thickness of the particle walls and active surface area were investigated with images analysis. A brief description is given here, and a more

detailed description of the methods used for image analyses is provided in Strandberg et al. [18]. The images were processed with binary segmentation, which transforms the grey level images into a binary model. Each pixel within the threshold gets a value of 1, and all other pixels get 0. The thresholding was selected with manual segmentation using visually selected threshold values, and the samples were divided into a solid material (ash) and air (pores and background). The pore volume consisted of pores connected with the background (named open pores) and closed pores (named discrete pores) completely encased in the ash particles.

To study the average particle walls thickness, a distance map algorithm (Chamfer Distance Map) was used on the ash. The average distance was calculated between pores and/or particle surfaces.

A polygonal surface mesh was generated for the ash without smoothing or simplifications before surface area analysis. A specific surface area was calculated by dividing the surface area by the volume of the ash.

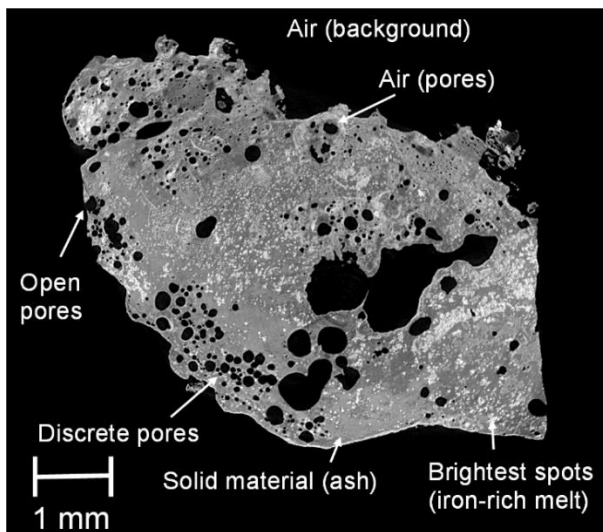


Figure 1. A microtomography slice showing a cross-section of BSB70 replicate 1, with arrows pointing to features discussed in the text.

Results and discussion

Pellets were fed into the burner without any problems. During sludge combustion, there were higher levels of SO_2 and NO_2 in the flue gases. It was dependent on the content of N and S in the fuel, with the highest measured levels for biosludge. Slag was formed in all combustion experiments. The amount increased with a higher proportion of sludge. BSB70, with 64 wt% of the ash in the form of slag, had the highest level, followed by MSB70 with 53 wt%. The slag particles from the burner grate and the bottom ash under the size of 1.4 mm were the fractions with the largest amounts, which therefore are the ones that would dominate in any ash recycling. Significant quantities of unburnt material (carbon) were found in the bottom ash, especially for the larger fractions. There was no cyclone ash at any of the runs, but deposits were found on heat exchangers.

Table 1 and Table 2 display the average relative composition in the slag respective bottom ash fraction ash under the size of 1.4 mm. A high amount of P was found in the slag from the mixed fuel, with a higher amount in the biosludge than mixed sludge and an increased amount with

more sludge in the fuel mixture. Bottom ash had lower P content overall, with less clear trends between fuel mixtures. High alkali content (K, Na) was found for all fuels.

Table 1. Average relative composition of the main ash forming elements in the slag formed in the burner on a C and O free basis.

		B100		MSB90		MSB70		BSB90		BSB70	
		Average	Stdev								
K	At%	9.8	1.1	9.7	0.9	7.0	0.2	9.0	0.1	6.6	0.1
Na		1.7	0.1	4.1	0.3	6.5	0.2	5.4	0.1	9.9	0.2
Ca		32.4	0.6	24.8	0.4	21.1	0.5	24.8	0.1	21.1	0.2
Mg		5.3	0.3	3.8	0.2	2.9	0.0	3.6	0.1	2.4	0.1
Mn		1.3	0.1	1.0	0.1	0.8	0.1	1.5	0.0	1.7	0.1
Fe		2.0	0.1	7.6	0.2	12.1	0.4	12.8	0.3	19.6	0.3
Al		10.4	0.5	9.7	0.6	9.4	0.1	8.1	0.1	6.4	0.6
Si		33.4	1.1	33.9	1.6	33.7	0.9	28.0	0.2	22.5	0.2
P		3.3	0.2	4.4	0.4	5.8	0.1	6.2	0.1	9.0	0.1
S		0.1	0.1	0.7	0.7	0.5	0.2	0.4	0.1	0.7	0.1

Table 2. Average relative composition of the main ash forming elements in the bottom ash under the size of 1.4 mm on a C and O free basis.

		B100		MSB90		MSB70		BSB90		BSB70	
		Average	Stdev								
K	At%	20.5	1.1	15.9	5.3	12.6	2.3	18.3	2.3	12.9	2.2
Na		2.2	0.2	3.7	1.3	6.1	1.4	3.6	0.5	7.8	1.8
Ca		38.6	2.1	28.7	9.7	26.3	2.1	31.8	2.9	22.8	1.9
Mg		7.0	0.5	5.4	1.9	4.9	0.6	6.6	1.2	4.5	0.7
Mn		2.0	0.2	1.6	0.5	1.6	0.2	2.3	0.2	2.2	0.3
Fe		3.0	0.5	8.4	6.2	12.6	3.3	6.7	1.2	15.8	2.3
Al		8.1	0.8	6.6	2.2	6.3	0.6	3.3	0.7	3.7	0.5
Si		10.5	2.7	10.7	5.1	15.0	3.9	14.5	5.1	13.0	1.9
P		4.8	0.4	5.0	1.7	5.1	0.7	3.9	0.3	5.6	0.8
S		2.2	0.3	5.2	1.8	8.7	1.2	6.8	0.9	10.1	1.3
Cl		0.9	0.2	0.7	0.8	0.8	0.4	2.3	0.7	1.5	1.3

With XRT, the slag particles could be investigated in 3D with high resolution. Examples of ash particle cross-sections are shown in the left column in Figure 2, discrete and open pores in the middle column, and a 3D reconstruction in the right column.

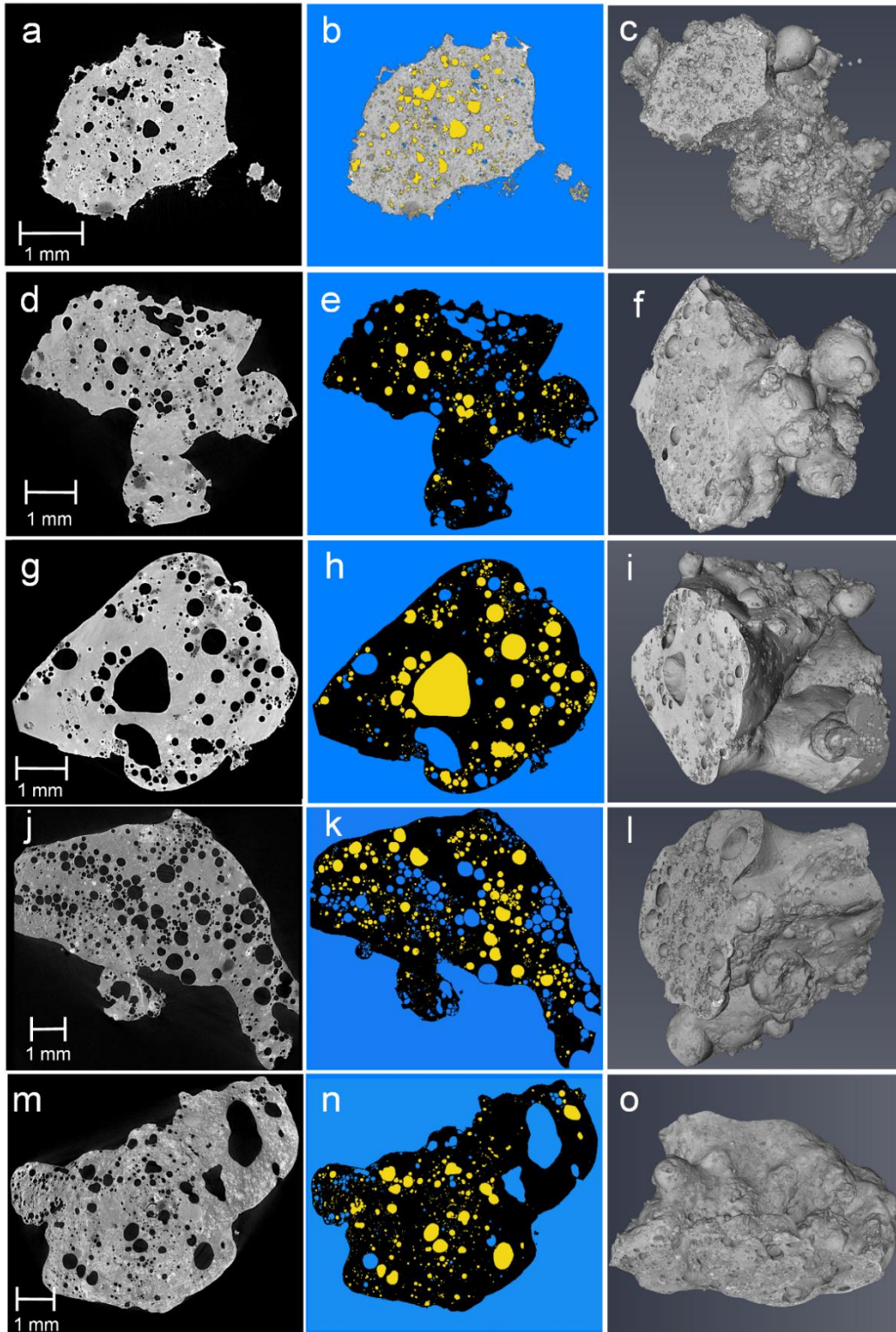


Figure 2. Results from XRT scanning of slag particles from the combustion of a-c) B100, d-f) MSB90, g-i) MSB70, j-l) BSB90, and m-o) BSB70. The left column shows X-ray tomography cross-sections of ash particles; the middle column cross-section shows the pores, where the ash particle is black, and the background and open pores are coloured bright blue and discrete pores yellow. The right column shows 3D reconstructions of the particles. Grayscale is set after X-ray attenuation (optical density), where brighter parts have high optical density.

The specific surface area was calculated as the surface area per volume to enable comparison between different sizes of particles. No clear trends were seen for the surface area, with the average specific surface area varying between 11 and 18 mm²/mm³. The specific surface area seems to be slightly lower than previous work on wheat straw and sewage sludge ash and mixtures of those; mixed wheat straw and sewage sludge had a specific surface area of 17–27 mm²/mm³ and pure wheat straw 31–34 mm²/mm³ [18]. This despite a lower resolution in that study, which according to Hyväluoma et al. affects the specific surface area by limiting small pores and wall roughness visibility [19].

The porosity was calculated for each particle and averaged for each type of slag. MSB70 had the highest average porosity with 23 vol% and the highest open pore volume (56 vol%). The other mixed samples had comparable porosity of 17-18 vol%, and B100 had the lowest porosity with a 12 vol% on average. B100 also had the lowest open pore volume with 12 vol%. Wheat straw ash and ash from wheat straw and sewage sludge had higher porosity, with an average of 62 vol% for wheat straw and 29-31 vol% for the mixtures [18]. The open-pore volume was also high for those samples (72-99 vol%). While B100 had the lowest porosity and open-pore volume, it had the most significant number of discrete pores per particle volume, indicating many tiny pores. The number of discrete pores per particle volume is high for ash from bark and biosludge mixtures with 5827-1310 counts/mm³.

Unlike the previously examined wheat straw and sewage sludge ash, these particles have few and small pore openings at the outer surface, most of them with a size of 50-100 μm or less, and relatively thick particle walls. For some particles, there were some larger openings of 300-500 μm. There are larger openings in areas where the ash has been broken, some of them in size of 300-500 μm. Based on this, it can be assumed that roots have difficulty getting into particles that are not crushed in their search for nutrients.

Table 3. Results from image analysis, as average from three replicate, with the specific surface area, sample porosity, open-pore volume, number and size of discrete pores, and average wall thickness.

	Specific surface area [mm ² /mm ³]	Sample Porosity [vol%]	Open pore volume [vol%]	No. of discrete pores/per particle volume [counts/mm ³]	Mean equivalent pore diameter of discrete pores [μm]	Wall thickness [μm]
B100	14	12	12	5827	14	51
MSB90	18	18	48	4267	14	59
MSB70	17	23	56	1387	13	75
BSB90	12	18	39	1653	17	82
BSB70	11	17	39	1310	19	110

The distribution of the size of discrete pores has been evaluated based on the equivalent diameter and classified by the definition of the Soil Science Society of America [20] and the criteria proposed by Cameron and Buchan [21]. The pores were divided into size ranges were 0.1-5 μm are classified as ultramicropores, 5-30 μm as micropores, 30-75 μm as mesopores, and >75 μm as macropores. Table 4 shows the counts divided by the total number of discrete pores and the volume distribution as the volume share of the total pore volume of discrete pores. The most significant relative number of pores were classified as micropores. However, due to the resolution, the smallest pores here has an equivalent diameter of 3.8 μm. The share of the number of pores might look different with a higher resolution and then reach even smaller pores. In terms

of volume, the largest volume share of pores consists of macropores. Soil research has shown that small pores with a minimum equivalent diameter under 30 μm store water while larger pores transmit water [21].

Table 4. Pore size distribution for discrete pores, divided into size ranges, showing the relative number of pores and relative pore volume as an average.

EqDiameter	B100		MSB90		MSB70		BSB90		BSB70	
	Average	Stdev								
Relative number of pores										
0.1-5 μm	0.16	0.01	0.19	0.03	0.34	0.21	0.15	0.03	0.12	0.01
5-30 μm	0.76	0.01	0.74	0.01	0.58	0.04	0.73	0.01	0.74	0.01
30-75 μm	0.06	0.01	0.06	0.02	0.06	0.03	0.10	0.02	0.12	0.00
> 75 μm	0.01	0.00	0.01	0.00	0.01	0.02	0.02	0.01	0.02	0.00
Relative pore volume										
0.1-5 μm	0.00	0.00	0.00	0.00	0.00	0.00	0.00	0.00	0.00	0.00
5-30 μm	0.06	0.01	0.06	0.02	0.04	0.02	0.02	0.01	0.02	0.00
30-75 μm	0.13	0.02	0.13	0.02	0.11	0.05	0.08	0.02	0.08	0.02
> 75 μm	0.81	0.03	0.81	0.03	0.85	0.08	0.90	0.03	0.90	0.02

Conclusions

Nutrient amounts indicate that the slag from the combustion of 30% biosludge and 70% bark can be useful as a soil improver directly or for a further refinery. The P content was 9 at% on a C and O free basis. Morphology of the slag particles was analysed with synchrotron-based X-ray microtomography at a micrometre scale. The porosity of the slag varied between 17-23_{vol}% for the bark and sludge mixtures, and 39-56_{vol}% was open pores connected to the surrounding volume. The number of discrete pores per particle volume is overall high for ash from bark and biosludge mixtures. The largest relative number of discrete pores were classified as micropores (5-30 μm), but the largest volume share of discrete pores consists of macropores (>75 μm). The slag particles have relatively thick walls, with few pore openings to the surroundings, indicating that the slag needs to be grounded before application in the soil for improving the roots accesses to the nutrients.

Project Outcomes

This result will be published in a scientific article in the coming months. One more paper is planned based on tomography data gained at the Synchrotron SOLEIL of the ash at higher resolution and phosphate distribution. The results were also intended to be presented at a conference, with participants from academia and from industry and/or the public sector. Due to the pandemic, this has not been possible, but we plan to do so in the future.

Acknowledgements

We acknowledge the Synchrotron SOLEIL for the provision of synchrotron radiation facilities and Dr Jonathan Perrin for assistance in using beamline ANATOMIX (proposal No. 20201693). ANATOMIX is an Equipment of Excellence (EQUIPEX) funded by the Investments for the Future program of the French National Research Agency (ANR), project NanoimagesX, grant no. ANR-11-EQPX-0031.

The facilities and technical support (Dr Cheng Choo Lee) of the Umeå Core Facility for Electron Microscopy (UCEM) at the Chemical Biological Centre (KBC), Umeå University, National Microscopy Infrastructure, NMI (VR-RFI 2016-00968), are also acknowledged.

The authors want to thank Anna Ramberg and Jörg Brücher at Holmen AB for the help and provision of sludges. The authors also wish to acknowledge Gunnar Kahlén and Markus Segerström at Biomass Technology Centre, Department of Forest Biomaterials and Technology, Swedish University of Agricultural Sciences, for grinding, mixing and pelletising the fuels and help with the combustion experiments. Bark and chemical analysis of bark were received from the MOBILE FLIP project, which received funding from the European Union's Horizon 2020 research and innovation program under grant agreement number 637020–MOBILE FLIP.

Finally, the ÅForsk Foundation are greatly acknowledged for financing this work.

References

- [1] COMMUNICATION FROM THE COMMISSION TO THE EUROPEAN PARLIAMENT, THE COUNCIL, THE EUROPEAN ECONOMIC AND SOCIAL COMMITTEE AND THE COMMITTEE OF THE REGIONS on the 2017 list of Critical Raw Materials for the EU COM/2017/0490 final, in, <https://eur-lex.europa.eu/legal-content/EN/TXT/?uri=CELEX:52017DC0490>, European Commission 2017.
- [2] Cepi, KEY STATISTICS 2019 European pulp & paper industry, in, <https://www.cepi.org/wp-content/uploads/2020/07/Final-Key-Statistics-2019.pdf>, 2019.
- [3] Directive (EU) 2018/850 of the European Parliament and of the Council of 30 May 2018 amending Directive 1999/31/EC on the landfill of waste, in, Official Journal of the European Union <https://eur-lex.europa.eu/legal-content/EN/TXT/?uri=celex%3A32018L0850>, 2018.
- [4] Council Directive 1999/31/EC of 26 April 1999 on the landfill of waste, in, <https://eur-lex.europa.eu/legal-content/EN/TXT/?uri=CELEX%3A01999L0031-20180704>, 2018.
- [5] N. Skoglund, A. Grimm, M. Ohman, D. Boström, Combustion of biosolids in a bubbling fluidised bed, part 1: main ash-forming elements and ash distribution with a focus on phosphorus, *Energy Fuels*, 28 (2014) 1183-1190.
- [6] J. Werther, T. Ogada, Sewage sludge combustion, *Prog. Energy Combust. Sci.*, 25 (1999) 55-116.
- [7] W. Rulkens, Sewage sludge as a biomass resource for the production of energy: overview and assessment of the various options, *Energy Fuels*, 22 (2007) 9-15.
- [8] L. Eriksson, R. Njurell, A. Eklund, Supplying of sludge from the paper-and pulp industry to furnaces. Step 3-design before full-scale tests; Tillfoersel av skogsindustriellt slam till eldstaeder. Etapp 3-Projektering infoer fullskalefoersoek, in, Vaermeforsk, Stockholm (Sweden), 2003.
- [9] J. Dahlbom, R. Wadsborn, Effects of Non Process Elements in the chemical recovery system of paper mills; Effekter av PFG foer integrerade pappersbruk vid indunstning och foerbraenning av bioslam i sodapannan, in, Vaermeforsk, Stockholm (Sweden), 2005.
- [10] M. Van de Velden, R. Dewil, J. Baeyens, L. Josson, P. Lanssens, The distribution of heavy metals during fluidised bed combustion of sludge (FBSC), *J. Hazard. Mater.*, 151 (2008) 96-102.
- [11] A. Grimm, J. Etula, R. Salh, G. Kalén, M. Segerström, J. Brücher, C. Söderberg, D. Soukup, C. Pfeifer, S.H. Larsson, Slagging and fouling characteristics during co-combustion of Scots pine bark with low-temperature dried pulp and paper mill chemical sludge, *Fuel Process. Technol.*, 193 (2019) 282-294.
- [12] T. Weitkamp, M. Scheel, J.L. Giorgetta, V. Joyet, V. Le Roux, G. Cauchon, T. Moreno, F. Polack, A. Thompson, J.P. Samama, The tomography beamline ANATOMIX at Synchrotron SOLEIL, *Journal of Physics: Conference Series*, 849 (2017) 012037.
- [13] A. Mirone, E. Brun, E. Gouillart, P. Tafforeau, J. Kieffer, The PyHST2 hybrid distributed code for high speed tomographic reconstruction with iterative reconstruction and a priori knowledge capabilities, *Nuclear Instruments and Methods in Physics Research Section B: Beam Interactions with Materials and Atoms*, 324 (2014) 41-48.
- [14] D. Paganin, S.C. Mayo, T.E. Gureyev, P.R. Miller, S.W. Wilkins, Simultaneous phase and amplitude extraction from a single defocused image of a homogeneous object, *Journal of Microscopy*, 206 (2002) 33-40.

- [15] T. Weitkamp, D. Haas, D. Wegrzynek, A. Rack, ANKAphase: software for single-distance phase retrieval from inline X-ray phase-contrast radiographs, *Journal of synchrotron radiation*, 18 (2011) 617-629.
- [16] C.A. Schneider, W.S. Rasband, K.W. Eliceiri, NIH Image to ImageJ: 25 years of image analysis, *Nature methods*, 9 (2012) 671.
- [17] J. Schindelin, I. Arganda-Carreras, E. Frise, V. Kaynig, M. Longair, T. Pietzsch, S. Preibisch, C. Rueden, S. Saalfeld, B. Schmid, Fiji: an open-source platform for biological-image analysis, *Nature methods*, 9 (2012) 676.
- [18] A. Strandberg, N. Skoglund, M. Thyrel, Morphological characterisation of ash particles from co-combustion of sewage sludge and wheat straw with X-ray microtomography, *Waste Manage. (Oxford)*, 135 (2021) 30-39.
- [19] J. Hyväluoma, S. Kulju, M. Hannula, H. Wikberg, A. Kalli, K. Rasa, Quantitative characterisation of pore structure of several biochars with 3D imaging, *Environ Sci Pollut Res Int*, 25 (2018) 25648-25658.
- [20] Glossary of soil science terms 2008, in, Soil Science Society of America, Soil Science Glossary Terms Committee 2008.
- [21] K.C. Cameron, G.D. Buchan, Porosity: Pore Size Distribution, in: *Encyclopedia of soil science*, CRC Press, 2017, pp. 1782-1785.